Realization of the CNOT quantum gate operation in six-dimensional ammonia using the OCT-MCTDH approach

Markus Schröder[a] and Alex Brown[b]
Department of Chemistry, University of Alberta, Edmonton, Alberta T6G 2G2, Canada

(Received 15 April 2009; accepted 13 June 2009; published online 15 July 2009)

Comparative studies of implementations of the controlled NOT quantum gate operation using vibrational states of ammonia as the qubit states are presented. The quantum gate operations are realized using tailored laser pulses, which are calculated using a combined approach of optimal control theory and the multiconfiguration time-dependent Hartree method. We compare results obtained with a reduced model of ammonia with three degrees of freedom (all N–H bond distances fixed) to those obtained with a full six-dimensional model. In our study, the optimal laser pulses of both models induce similar underlying physical mechanisms while the gate quality within the reduced model (>98%) is much higher than within the six-dimensional model (≈80%).
 [DOI: 10.1063/1.3168438]

I. INTRODUCTION

In recent years, optimal control theory (OCT) has gained growing interest, theoretically and experimentally, as a method for obtaining tailored laser pulses to manipulate the dynamics of quantum systems.[1–8] The ability to influence the system's dynamics in a controlled manner opens a wide range of applications, such as the optimization of product channels in chemical reactions or spectroscopic studies of (otherwise) hidden transitions through selectively suppressing or enhancing the population of states.[9] In particular, de Vivie-Riedle and Tesch[10] proposed the use of OCT for implementing quantum gate operations using vibrational modes of molecules. Several theoretical publications followed this suggestion, most of them utilizing either diatomic[11–14] molecules or reduced dimensionality polyatomic models, e.g., acetylene[10,15,16] and ammonia.[17] For example, in Ref. 17, a two-dimensional model of ammonia, covering the symmetric bending and asymmetric bending modes, has been utilized to implement quantum gate operations.

The main challenge in theoretical as well as in experimental studies is to find the optimal laser pulse that leads to the desired outcome. Several numerical methods, such as iterative and genetic algorithms,[18–20] have been employed to achieve this goal, while in experiments usually only genetic algorithms are used. For theoretical studies, the main difficulty arises from the fact that most algorithms require repeated and explicit solution of the time dependent Schrödinger equation (TDSE) for the system. This is only possible for small systems with a few degrees of freedom (DOF). For larger systems, such as molecules with many DOFs, this is difficult or even impossible, if direct methods for solving the TDSE are applied. Nevertheless, there have been several experimental as well as theoretical studies in obtaining optimal laser pulses for polyatomic molecules. Within the theoretical studies, however, one is usually limited to treating only a subsystem of the complete molecule exactly or to use effective models of lower dimensionality. This immediately raises the question whether such approximate descriptions of large molecules can serve as model systems to predict the optimal pulses and the optimization outcome with sufficient accuracy to serve as a starting point for experimental studies or to interpret experimental results. Comparative studies of model systems with and without approximations can answer this question.

A way to overcome the numerical drawback of solving the TDSE for large systems is the application of approximate methods such as the multiconfiguration time-dependent Hartree (MCTDH) method.[21–24] Within the MCTDH approach, the multidimensional wave function is approximated with a set of low-dimensional but time-dependent basis functions, as opposed to time-independent basis functions used in standard methods, which are defined only in a subset of the systems DOF (for a review see, e.g., Ref. 23). Within the MCTDH approach, propagating the wave function requires much less memory and computation time for systems with multiple DOF. In addition, as a variational method, MCTDH converges toward the exact wave function as more time-independent basis functions are taken into account. Therefore, the accuracy of a wave function can be readily checked.

In the present paper, we use the combination of OCT and MCTDH[16,25] to investigate the implementation of quantum gate operations using vibrational states of ammonia as the qubit basis. Ammonia has been suggested previously[17] as a potential candidate molecule for quantum computing based on a reduced two-dimensional model. In particular, we compare results obtained with a reduced model containing only three relevant DOF to a model comprising all six internal DOF of ammonia. This allows us to assess the use of a reduced dimensional model to predict the controllability of a full dimensional model (for the vibrational modes).

[a]Present address: Theoretische Chemie, Universität Heidelberg, Im Neuenheimer Feld 229, D-69120 Heidelberg, Germany. Electronic mail: markus.schroeder@pci.uni-heidelberg.de.
[b]Electronic mail: alex.brown@ualberta.ca.

The paper is organized as follows: In Sec. II we briefly review MCTDH and OCT and in Sec. III the model system is introduced. In Sec. IV, the numerical calculations are presented and discussed. A brief summary and future outlook are given in Sec. V.

II. THE OCT-MCTDH APPROACH

A. Combining OCT and MCTDH

The equation of motion (EOM) of a quantum mechanical state is given by the TDSE, i.e., the evolution in time of a given state $|\Psi\rangle$ is governed by the system Hamiltonian H, which, in general, may be time dependent. Treating the interaction of the system with an external light source semiclassically and within the dipole approximation, the TDSE reads ($\hbar$ is set to unity throughout the paper)

$$\frac{\partial}{\partial t}|\Psi(t)\rangle = -iH(t)|\Psi(t)\rangle = -i(H_0 - \mu E(t))|\Psi(t)\rangle, \tag{1}$$

where H_0 is the Hamiltonian of the unperturbed system, μ is the dipole operator, and E denotes the electric (laser) field.

Given an initial state $|\Psi_0\rangle = |\Psi(t_0)\rangle$ at the initial time t_0 and the system Hamiltonian (i.e., in particular the electric field), one usually seeks to calculate the system state at some later time $t > t_0$. For notational convenience we set $t_0 = 0$ in the following. On the contrary, within OCT one is interested to find the electric field that would drive the system state to a desired outcome, i.e., to maximize the expectation value of a given target operator $\hat{O}$ at a given time $T > 0$, where $\hat{O}$ is positive semidefinite. The target operator could, for instance, be a projection onto a given target state or a product channel of a chemical reaction. In order to find the electric field that maximizes the target, one defines a control functional J for example as

$$\begin{aligned} J(E,T) &= \langle\Psi(T)|\hat{O}|\Psi(T)\rangle - \alpha\int_0^T dt\frac{(E(t))^2}{S(t)} \\ &= J_1(E,T) - J_2(E,T). \end{aligned} \tag{2}$$

The control functional given in Eq. (2) consists of two parts: J_1 to maximize the expectation value of the target and J_2 penalizing for the overall field strength. Here α serves as a penalty factor and $S(t)$ denotes the shape function that can be used to enforce smooth pulse envelopes. The control functional given in Eq. (2) does not contain any side conditions. Often one adds a third term J_3 to ensure that the system state evolves according to the TDSE [this is implicitly assumed in Eq. (2)], but also further constraints, e.g., on the field,[26] may be applied. In the present case we used a modified J_1 in order to account for multiple targets $\hat{O}_i$, which can be optimized by defining J_1 as a sum over targets, i.e., as

$$J_1(E,T) = \sum_i \langle\Psi_i(T)|\hat{O}_i|\Psi_i(T)\rangle. \tag{3}$$

Variation of the control functional Eq. (2) with respect to $E(t)$ leads to an expression for the optimal field,

$$E(t) = -\frac{S(t)}{\alpha}\sum_i \mathrm{Im}\langle\Theta_i(t)|\mu|\Psi_i(t)\rangle, \tag{4}$$

where $|\Theta_i(t)\rangle$ is the backward propagated ith target state, which evolves according to the TDSE (1) with the initial condition $|\Theta_i(T)\rangle = \hat{O}_i|\Psi_i(T)\rangle$. Note that the right hand side of Eq. (4) also contains the field as part of the time-evolution operators acting on the system states. As a consequence, the optimal field E has, in general, to be obtained iteratively by successive propagations of the state vectors. Starting with an initial guess, the field is then constantly improved over the iterations. A number of algorithms, many of them monotonically convergent, has been proposed to most effectively obtain the optimized field.[3,4,27,28]

All of the proposed algorithms, however, involve solving the TDSE multiple times, which, as mentioned in the introduction, can be numerically very demanding or even impossible. Wang *et al.*[25] therefore proposed the use of the MCTDH approach to approximately solve the TDSE. One of the advantages of the MCTDH ansatz is that the quality of the approximation can be chosen almost arbitrarily. In Ref. 16, it was shown that monotonic convergence of the control functional is achieved for sufficient accuracy of the state vector. Within the MCTDH ansatz the wave function is approximated as

$$|\Psi(t)\rangle \approx \sum_{i_1}^{N_1}\sum_{i_2}^{N_2}\cdots\sum_{i_M}^{N_M} A_{i_1,i_2,\ldots,i_M}(t)\prod_j |\phi_{i_j}(q_j,t)\rangle. \tag{5}$$

The state vector $|\Psi\rangle$ is expressed in terms of time-dependent basis functions $|\phi_{i_j}(q_j,t)\rangle$, the so-called single-particle functions (SPFs), which are exclusively defined in single (or a few) modes with coordinates q_j, and the time-dependent coefficients A. The N_j therefore denotes the number of SPF used in the jth mode. The fact that the SPFs are time dependent allows for the use of a small number of coefficients (i.e., small N_j) such that the number of coefficients is usually much smaller than in standard methods. At the price, however, that now a set of coupled EOM for the coefficients as well as the SPF has to be solved (see, e.g., Ref. 23). Inserting Eq. (5) into Eq. (4) leads to an expression for the electric field within the MCTDH approach.

B. Implementation of OCT-MCTDH

The basic implementation of OCT into the Heidelberg MCTDH software package has been described previously.[16,25] We have now implemented a number of additional features into the OCT-MCTDH software relative to the previous versions. In particular, we ported the script that controls the iterative propagations to Python. We provide modules for basic parsing and wrapping of the input and operator files which allow reading, writing, and manipulation of input data. The modular structure of the optimal control script furthermore allows inclusion of future modules that may execute different algorithms such as genetic algorithms or algorithms that impose constraints (filters) on the field.

Our implementation now uses definitions of analytic expressions for the initial guess field, the shape function S [cf., Eq. (2)], etc. In particular, all analytic one-dimensional functions implemented in the MCTDH operator library can be used to define time-dependent functions used in the optimal control algorithms. This also includes sampled data. Similar to operators, different functions can be defined in the operator file and addressed via a user-defined label.

For target states (as opposed to target operators) we provide an option to use time-dependent overlaps as suggested by Zhu and Rabitz[29] to calculate the field. Furthermore, additional data may be written to output files, such as the time-dependent dipole matrix element [cf., Eq. (4)] or the time-dependent overlaps and target populations. We provide implementation for MCTDH version 8.4. We hope that our code will be made available as part of one of the future releases of the Heidelberg MCTDH software package.

III. MODEL SYSTEM

The choice of the set of coordinates to represent a polyatomic molecule is in many cases not an easy task and usually is highly adapted to the system under consideration. Several sets of coordinates have been used for ammonia and similar molecules (cf., Ref. 30 for a review). Usually, this leads to rather complicated and numerically problematic expressions for the kinetic energy operator. Recently, Gatti and co-workers published[30,31] a general but compact expression for the kinetic energy operator in curvilinear coordinates and applied it—among other polyatomic molecules—to a number of tetra-atomic molecules such as HONO, HFCO, H_2CS, and NH_3.[30–32]

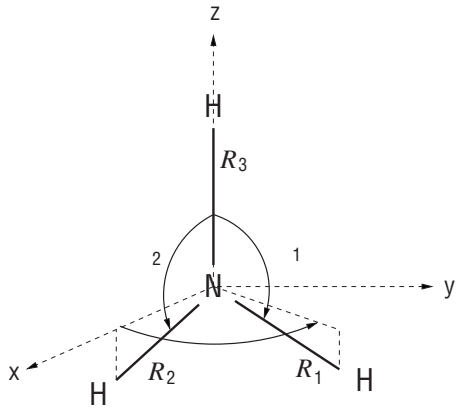

FIG. 1. Body-fixed coordinates of NH_3.

In the present contribution, we restrict ourselves to the description of the internal DOF of the ammonia molecule, i.e., we do not take into account global rotations of the molecule. This limits, of course, the comparability of our results to experimental findings, as we "choose" a fixed orientation of the molecule in the laboratory system and a polarization of the laser field. Using the formalism of Gatti and coworkers for ammonia, the set of coordinates involves the three distances R_i of the hydrogen atoms to the nitrogen atom, two bond angles θ_i, and one dihedral angle ϕ as depicted in Fig. 1. The kinetic energy operator then reads[32]

$$
\begin{aligned}
T = &- \sum_{i=1}^{3} \frac{M_{ii}}{2} \frac{\partial^2}{\partial R_i^2} - \sum_{i=1}^{2} \left[M_{i3} \xi_i \left(\frac{\partial^2}{\partial R_3 \, \partial R_i} + \frac{1}{R_3 R_i} \right) + \left(\frac{M_{ii}}{2R_i^2} + \frac{M_{33}}{2R_3^2} \right) \frac{\partial}{\partial \xi_i} u_i^2 \frac{\partial}{\partial \xi_i} \right] - M_{12} (\xi_1 \xi_2 + u_1 u_2 \cos\phi) \left(\frac{\partial^2}{\partial R_1 \, \partial R_2} + \frac{1}{R_1 R_2} \right) \\
&- \sum_{i=1}^{2} \left(\frac{M_{i3}}{2R_3} \frac{\partial}{\partial R_i} + \frac{M_{i3}}{2R_i} \frac{\partial}{\partial R_3} \right) \left(u_i^2 \frac{\partial}{\partial \xi_i} + \frac{\partial}{\partial \xi_i} u_i^2 \right) - \sum_{i,j=1}^{2,i\neq j} \left[\frac{M_{i3} u_i \cos\phi}{2R_3} \frac{\partial}{\partial R_i} \left(u_j \frac{\partial}{\partial \xi_j} + \frac{\partial}{\partial \xi_j} u_j \right) + \frac{M_{ij} \xi_i}{2R_j} \frac{\partial}{\partial R_i} \left(u_j^2 \frac{\partial}{\partial \xi_j} + \frac{\partial}{\partial \xi_j} u_j^2 \right) \right] \\
&- \frac{M_{33} \cos\phi}{2R_3^2} \left(u_1 \frac{\partial^2}{\partial \xi_1 \, \partial \xi_2} u_2 + u_2 \frac{\partial^2}{\partial \xi_1 \, \partial \xi_2} u_1 \right) + \sum_{i,j=1}^{2,i\neq j} \frac{M_{ij}}{2R_j} \frac{\partial}{\partial R_i} (u_i \cos\phi) \left(\xi_j u_j \frac{\partial}{\partial \xi_j} + \frac{\partial}{\partial \xi_j} \xi_j u_j \right) \\
&+ \sum_{i,j=1}^{2,i\neq j} \frac{M_{i3} \cos\phi}{2R_3 R_i} \left(u_j \frac{\partial^2}{\partial \xi_j \, \partial \xi_i} \xi_i u_i + \xi_i u_i \frac{\partial}{\partial \xi_j \, \partial \xi_i} u_j \right) + \sum_{i,j=1}^{2,i\neq j} \left[\frac{M_{i3}}{R_3 R_i} \frac{\partial}{\partial \xi_i} u_i^2 \xi_i \frac{\partial}{\partial \xi_i} + \left(\frac{M_{ij}}{2R_j} - \frac{M_{i3} \xi_j}{2R_3} \right) \frac{u_i}{u_j} \frac{\partial}{\partial R_i} \right. \\
&\left. \times \left(\sin\phi \frac{\partial}{\partial \phi} + \frac{\partial}{\partial \phi} \sin\phi \right) \right] - \frac{M_{12}}{2R_1 R_2} \left[\left(\frac{\partial}{\partial \xi_1} u_1 \xi_1 u_2 \xi_2 \frac{\partial}{\partial \xi_2} + u_1 \xi_1 \frac{\partial^2}{\partial \xi_1 \, \partial \xi_2} u_2 \xi_2 \right) \cos\phi + \frac{\partial}{\partial \xi_1} u_1^2 u_2^2 \frac{\partial}{\partial \xi_2} + u_1^2 \frac{\partial^2}{\partial \xi_1 \, \partial \xi_2} u_2^2 \right] \\
&+ \sum_{i,j=1}^{2,i\neq j} \frac{M_{i3} \xi_j}{2R_3 R_i u_j} \left(\sin\phi \frac{\partial^2}{\partial \xi_i \, \partial \phi} \xi_i u_i + \xi_i u_i \frac{\partial^2}{\partial \xi_i \, \partial \phi} \sin\phi \right) + \sum_{i,j=1}^{2,i\neq j} \frac{M_{ij}}{2R_i R_j u_j} \left(\frac{\partial}{\partial \xi_i} u_i \xi_i \sin\phi \frac{\partial}{\partial \phi} + u_i \xi_i \frac{\partial^2}{\partial \xi_i \, \partial \phi} \sin\phi \right) \\
&- \sum_{i,j=1}^{2,i\neq j} \left(\frac{M_{33} \xi_i}{2R_3^2 u_i} - \frac{M_{i3}}{2R_3 R_i u_i} \right) \left(\sin\phi \frac{\partial^2}{\partial \xi_j \, \partial \phi} u_j + u_j \frac{\partial^2}{\partial \xi_j \, \partial \phi} \sin\phi \right) - \sum_{i=1}^{2} \left(\frac{M_{ii}}{2R_i^2 u_i^2} + \frac{M_{33} \xi_i^2}{2R_3^2 u_i^2} - \frac{M_{i3} \xi_i}{R_3 R_i u_i^2} \right) \frac{\partial^2}{\partial \phi^2} \\
&- \left[\sum_{i,j=1}^{2,i\neq j} \frac{M_{i3} \xi_j}{R_3 R_i u_j u_i} - \frac{1}{u_1 u_2} \left(\frac{M_{12}}{R_1 R_2} + \frac{M_{33} \xi_2 \xi_1}{R_3^2} \right) \right] \frac{\partial}{\partial \phi} \cos\phi \frac{\partial}{\partial \phi}, \qquad (6)
\end{aligned}
$$

TABLE I. Qubit definitions and selected states with calculated (Calc.) as well as observed (Obs.) state energies relative to the ground state within the 3D and 6D models of ammonia.

					Energy (cm^{-1})				
Qubit state	Breath. ν_1	Inv. ν_2^p	Stretch. $\nu_3^{l_3}$	Bend. $\nu_4^{l_4}$	Calc. 3D (this work)	Calc. 6D (this work)	Calc. 6D (Ref. 33)	Obs.	Ref. (obs.)
$\|00\rangle$	0	1^+	0^0	0^0	903.07	933.12	932.50	932.43	36
$\|01\rangle$	0	2^-	0^0	0^0	1922.57	1882.80	1882.13	1882.18	37
$\|10\rangle$	0	1^+	0^0	1^1	2537.16	2539.79	2540.50	2540.53	38
$\|11\rangle$	0	2^-	0^0	1^1	3593.98	3502.56			
⋯	0	0^-	0^0	0^0	1.79	0.79	0.79	0.79	36
⋯	0	2^+	0^0	0^0	1548.81	1596.70	1597.46	1597.47	37
⋯	0	3^+	0^0	0^0	2454.31	2383.06	2384.15	2384.15	38
⋯	0	0^-	0^0	1^1	1668.73	1626.47	1627.40	1627.38	37
⋯	0	2^+	0^0	1^1	3183.74	3188.92			
⋯	0	3^+	0^0	1^1	4137.64	4007.76			

with $\xi_i=\cos\theta_i$, $u_i=\sin\theta_i$, and M_{ij} being the matrix elements of the inverse-mass matrix

$$\mathbf{M}=\begin{pmatrix} \frac{1}{m_H}+\frac{1}{m_N} & \frac{1}{m_N} & \frac{1}{m_N} \\ \frac{1}{m_N} & \frac{1}{m_H}+\frac{1}{m_N} & \frac{1}{m_N} \\ \frac{1}{m_N} & \frac{1}{m_N} & \frac{1}{m_H}+\frac{1}{m_N} \end{pmatrix}. \tag{7}$$

Here m_N and m_H denote the masses of the nitrogen and hydrogen atoms, respectively.

Note, that the kinetic energy operator, Eq. (6), is calculated for a volume element $dV=dR_1dR_2dR_3d\theta_1d\theta_2d\phi$, which results in additional potential terms (cf., Ref. 31). For the present calculations, we used an accurate potential energy surface (PES) and dipole surfaces for the electronic ground state that have been recently published.[33,34] While it was possible to use the PES as it is (except for a change in coordinates), it was necessary to fix the orientation of the molecule—hence the orientation of the dipole—with respect to the orientation of the polarization of the laser field. Otherwise global rotations of the molecule would have to be taken into account, too. For this purpose, we projected the dipole onto the normal vector of the plane spanned by the three hydrogen atoms (linear configurations are outside the sampled area). This results in an effective dipole surface with strong transition dipoles between states of the inversion mode.

In the following we compare results obtained with a reduced, three-dimensional (3D), model which was obtained by setting the three distances to their equilibrium values of 1.01 Å, i.e., the three stretching modes are removed from the model system, to the full six-dimensional (6D) model of ammonia. Accordingly, the model Hamiltonian of the reduced system is obtained from Eq. (6) by setting to zero all terms containing a differential operator with respect to one of the distances R_i. The exact 3D Hamiltonian can be obtained using the procedure discussed by Gatti and Iung,[35] but the model Hamiltonian used here provides sufficiently accurate results, see Sec. IV.

IV. RESULTS AND DISCUSSION

As mentioned above, Tesch and de Vivie-Riedle[10] proposed the use of vibrational DOF of polyatomic molecules as the physical basis and the use of tailored laser fields to perform quantum gate operations. This requires the definition of states to represent the basic units of quantum information, the qubits, within the set of all vibrational states of the molecule. In principle, any two orthogonal states of a quantum system can be labeled as $|0\rangle$ and $|1\rangle$, thus defining a qubit. For the generalization to n qubits one defines the qubits within different DOF of the system under consideration, e.g., as spins of different particles, to be able to manipulate and measure the qubits independently from each other. This then leads to a subspace spanned by 2^n basis states embedded in the complete system.

A. The qubit system

In the present case, the qubits are defined in different vibrational modes of the ammonia molecule. In particular, for the two-qubit operations, we define the qubits as excited states within the inversion and the asymmetric bending modes while keeping all other modes in the ground state. This choice of qubits also allows us to switch easily to a reduced dimensionality model. The details of the four states spanning the two-qubit systems, used in Sec. IV B, are given in Table I. Note that, of course, the quantum numbers associated with stretching modes do not apply for the 3D model.

The first qubit labels states from the asymmetric bending mode, while the second qubit labels excited states within the inversion mode with quantum numbers as outlined in Table I. Note that the quantum numbers $\nu_3^{l_3}$ and $\nu_4^{l_4}$ for asymmetric stretching as well as asymmetric bending each comprise two degenerate modes with l_i being the quantum number for the respective vibrational angular momentum.[33,39] The qubit system defined in Ref. 17 has been defined using states with more quanta of excitation in both the asymmetric bending as well as the inversion mode. As pointed out in Ref. 17 defining the set of qubits starting in the ground state can lead to difficulties for quantum gate operations like the Hadamard gate. On the other hand, it becomes more and more demanding to propagate higher-lying vibrational eigenstates with

TABLE II. Primitive grid used for the MCTDH calculations.

Coordinate	Range	Grid points	Primitive basis
R_i	0.66–1.48 Å	15	Harmonic oscillator
$\cos(\theta_i)$	−0.99 to 0.5	18	Sine
ϕ	0.8–5.48 rad	32	Harmonic oscillator

sufficient precision within MCTDH as more SPF are needed. The present choice of qubits constitutes a compromise between these considerations.

The vibrational eigenstates have been calculated using the *improved relaxation*[32] option of the MCTDH software, which prepares the initial wave functions in MCTDH form according to Eq. (5). For details of the setup used see Tables II–IV for the primitive grid of the 3D and 6D models, respectively. The PES and the effective dipole surface have been fit using POTFIT (Ref. 23) from the MCTDH software package. This became necessary since different internal coordinates have been used in Refs. 33 and 39. We used the *correlated weight* option with a cutoff at 20 000 cm^{-1} and using 15 iterations of optimization. The root-mean-square error of this setup for the 6D model has been 14.7 cm^{-1} for the PES in the relevant region. The dipole surface has been fit without the *correlated weight* option resulting in a root-mean-square error of 3.08×10^{-3} D. Of course, better fits are possible by taking into account more natural potentials, however, this significantly slows down the propagations using MCTDH as more operator terms would have to be evaluated. For the 3D model, the root-mean-square-errors for the PES and the dipole surface have been obtained as 2.85 cm^{-1} and 2.32×10^{-6} D, respectively.

The differences between the calculated energies of this work and those obtained from Ref. 33, see Table I, are probably due to the approximations made using POTFIT. Small errors can also be assigned to the approximations made by representing the state vector in MCTDH form and the primitive grid (cf., Table II). In general, the eigenenergies obtained with MCTDH using the setup shown in Table III are within a few wave numbers of those given in Ref. 33, where the differences become larger for higher-lying eigenstates above 3000 cm^{-1}.

B. Controlled NOT gate

The controlled NOT (CNOT) gate is defined as a two-qubit operation in which a target qubit is to be flipped when the control qubit is 1, otherwise, the states are to be left unchanged, i.e.,

TABLE III. Settings used for the MCTDH and POTFIT calculations for 6D-ammonia.

Combined modes	SPF		Natpot basis potential and dipole
	Relaxation	Propagation	
R_1, R_2	35	8	10
θ_1, θ_2	35	18	Contracted
ϕ, R_3	35	12	10

TABLE IV. Settings used for the MCTDH and POTFIT calculations for 3D-ammonia.

Modes	SPF		Natpot basis potential and dipole
	Relaxation	Propagation	
θ_1	15	9	12
θ_2	15	9	12
ϕ	15	9	Contracted

$$\begin{aligned} |00\rangle &\rightarrow |00\rangle \\ |01\rangle &\rightarrow |01\rangle \\ |10\rangle &\rightarrow |11\rangle \\ |11\rangle &\rightarrow |10\rangle. \end{aligned} \tag{8}$$

Here the first qubit serves as the control while the second qubit serves as the target. For the choice of qubits used in the present work, see Table I, the bending DOF serves as the control bit while the inversion mode is the target. The CNOT operation, Eq. (8), constitutes a multitarget optimization problem[10] for which the optimal field is determined according to Eqs. (3) and (4).

C. 3D-ammonia

In the following, we present results obtained with the reduced 3D model of ammonia. The algorithm has been started from an initial guess field of the form

$$E_{\text{guess}}(t) = E_0 \sin(\omega_{\text{guess}} t)\sin^2\left(\frac{\pi t}{T}\right), \tag{9}$$

with $E_0=308.5$ MV/m, $T=1$ ps, and $\omega_{\text{guess}}\simeq962$ cm^{-1}, where the frequency ω_{guess} has been chosen according to the energy difference between the $|11\rangle$ and $|10\rangle$ states for the 6D model, see Table I. The penalty factor has been set to $\alpha_0=3.782\times10^{-12}$ m^2/V^2 s=5.0 a.u., while the pulse envelope has been set to $S(t)=\sin^2(\pi t/T)$. The control algorithm converged after 100 iterations ($\Delta J\approx10^{-4}$ for two subsequent iterations) yielding an average target population of 99.2% as shown in Fig. 2. Note that the graph for J_1 in Fig. 2 accounts for the sum of the populations of all targets so that $J_1=4$

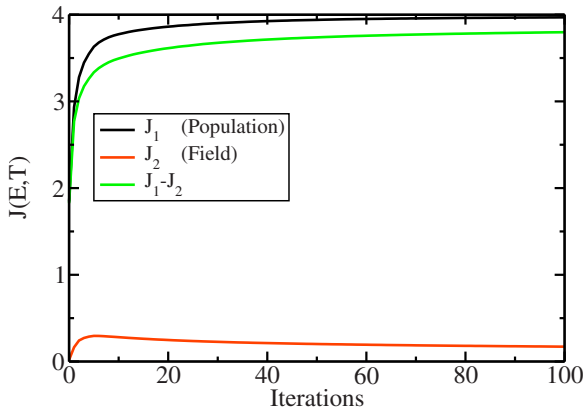

FIG. 2. Control functional as a function of iterations for the 3D model of ammonia ($J_1=4\equiv100\%$ population transfer for each target).

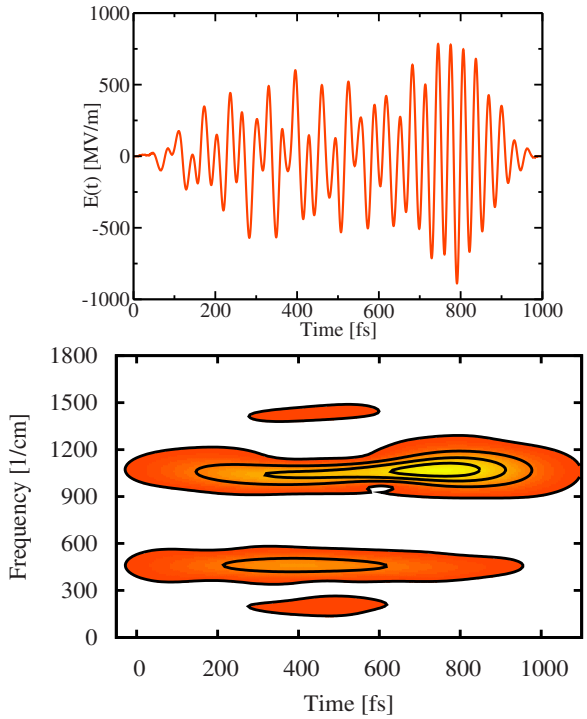

FIG. 3. Optimized field (upper) and its FROG trace (lower) after 100 iterations using the 3D model of ammonia.

would correspond to 100% population transfer for each of the four targets.

In Fig. 3, the optimal electric field after 100 iterations of the OCT algorithm for the CNOT gate is shown together with its XFROG trace.[40] The XFROG trace has been calculated as

$$I_{\mathrm{XFROG}}(\omega,t) = \left| \int_{-\infty}^{\infty} d\tau E(\tau) G(t-\tau) e^{-i\omega\tau} \right|^2, \tag{10}$$

with G being the so-called gate function which acts as a window to select parts of the signal around time t. In this case we chose $G(t)=\exp(-t^2/2\sigma^2)$ as a standard Gaussian with a width $\sigma \approx 108.8$ fs. This particular choice of $G(t)$ has been made to have a sufficiently broad gate function that covers several of the relatively few oscillations of the field while maintaining sufficient resolution in the time domain. The optimization within the 3D model yields a seemingly complex field with several frequency components. Besides the main contribution of the field, centered at approximately 1100 cm^{-1} in the frequency domain, several other contributions are visible in the XFROG trace. However, only the main contribution corresponds near the transition frequency between the states $|10\rangle$ and $|11\rangle$ of 1056.82 cm^{-1}.

Figure 4 outlines the population dynamics of the states with more than 1% population at any time during the optimal pulse. In Figs. 4(a) and 4(b), the population dynamics are shown for the initial states $|00\rangle$ and $|01\rangle$, respectively. One can see that there is little population transfer out of the qubit states. However there is a considerable transfer of population between the states $|00\rangle$ and $|01\rangle$, which vanishes at final time T. This is due to a strong transition dipole of 0.32 D between those states at a frequency of 1020 cm^{-1}.

In the case where $|10\rangle$ and $|11\rangle$ are the initial states, Figs. 4(c) and 4(d), almost a direct transition to the respective target state can be observed. At the final time T, the population of the target state is about 99% in both cases. As in the discussion of Figs. 4(a) and 4(b), population transfer to higher excited states of the inversion mode can be observed,

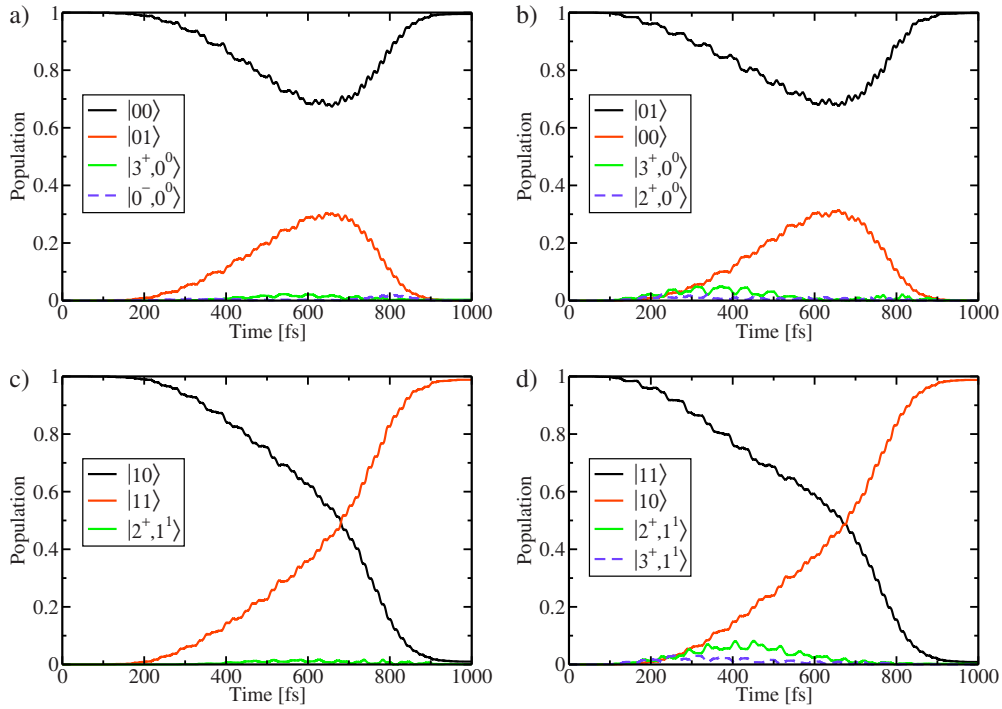

FIG. 4. Population of vibrational eigenstates of the 3D model of ammonia as a function of time. Curves are shown for all states with population ≥1%. Initial states are (a) $|00\rangle$, (b) $|01\rangle$, (c) $|10\rangle$, and (d) $|11\rangle$.

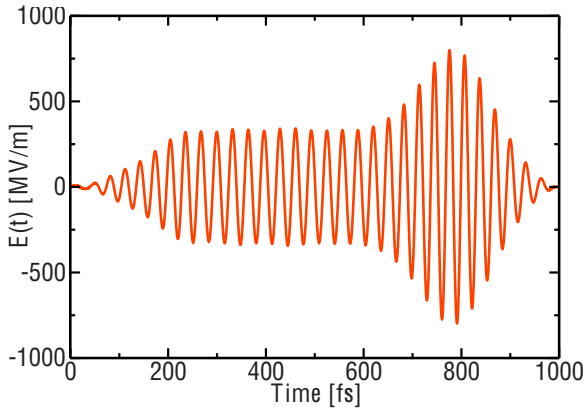

FIG. 5. Filtered optimized field using a 3D model of ammonia.

especially in Fig. 4(d), while the quantum number of the asymmetric bending mode is preserved due to selection rules.

It is interesting to note, however, that the frequency components, visible around 200, 500, and 1400 cm^{-1} in Fig. 3, are spurious, i.e., they are not needed for performing the gate operation. Filtering out these components with a band-pass filter that only lets through contributions between 900 and 1200 cm^{-1} leads to the field shown in Fig. 5. The filtered field contains a single central frequency and has a smooth pulse envelope. The system dynamics are steered by simply varying the field amplitude, not the frequency, to distinguish between the two competing transitions $|00\rangle \rightarrow |01\rangle$ and $|10\rangle \rightarrow |11\rangle$.

A propagation with the filtered field leaves the target population at the final time almost unchanged compared to propagation with the unfiltered field as shown in Fig. 6. The average target population has been obtained as 98.7%—about 0.5% lower than without filtering. The field part of control functional J_2 decreases from 0.170 (unfiltered) to 0.152 (filtered). It can also be observed that the transfer to other states is reduced compared to the unfiltered field. It should be noted that the transfer of population outside the two-qubit system using the unfiltered field is off-resonant with respect to the frequency components visible in Fig. 3. With the filtered field only in Fig. 6(a) with $|00\rangle$ being the initial state, some population is transferred to the asymmetric ground state of the inversion mode during the pulse. In all other cases, the population of states outside the two-qubit system is below 1%.

The spurious contributions seem to be generated through two-photon processes with a low resulting population transfer. This is possible since parts of the target are identical with the initial states, see Eq. (8). In the course of the iterations this can lead to an accumulation of small contributions generated by weak population transfer through off-resonant transitions. The spurious frequencies appear to be located in spectral regions between first-order transitions affecting populated states, in this case mainly the initial or target states. Relevant transitions near 500 cm^{-1} with significant transition dipole moments within the 3D model are $|11\rangle \rightarrow |2^+,1^1\rangle$ at 410 cm^{-1}, $|01\rangle \rightarrow |3^+,0^0\rangle$ at 532 cm^{-1}, and $|11\rangle \rightarrow |3^+,1^1\rangle$ at 543 cm^{-1} (cf., Table I), which are slightly below or above the spurious contribution at 500 cm^{-1}. In fact, for longer propagation times (5 ps), the spurious contribution appears at 470 cm^{-1}, i.e., in the center of the gap between 410 and 532 cm^{-1} (not shown here). The spurious contributions are initiated through the transitions at 532 cm^{-1} and especially at 543 cm^{-1} as small amounts of population are transferred already with the guess field. These contributions are then sustained through two-photon pro-

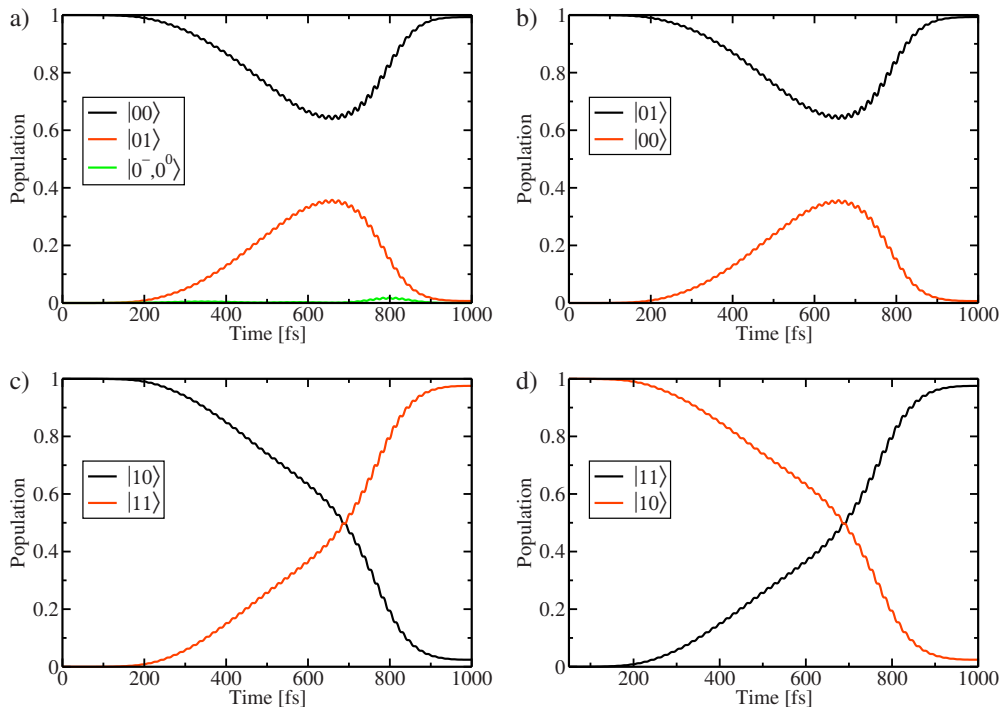

FIG. 6. Same as Fig. 4 but for the 3D model of ammonia using the filtered field of Fig. 3.

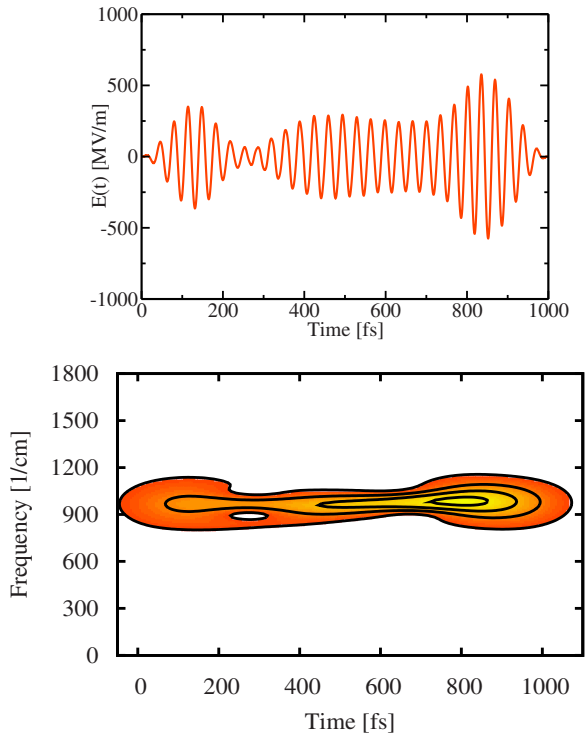

FIG. 7. Optimized field (upper) and its FROG trace (lower) after 50 iterations using the 6D model of ammonia.

cesses with zero population transfer. Removing the transitions at 532 and 543 cm^{-1} within an exact approach using eigenstates of the system Hamiltonian as a basis prevents the signal at 500 cm^{-1} from appearing (not shown here).

D. 6D-ammonia

In Fig. 7 the optimal electric field for the CNOT gate using the 6D model is shown. The field has been obtained after 50 iterations of the OCT algorithm, starting from the same initial guess field as in the 3D case and with the same penalty factor α and pulse envelope S. The control functional is shown in Fig. 8. $J(E)$ rapidly grows within the first few iterations and stagnates after about 40 iterations ($\Delta J \approx 10^{-3}$ for two subsequent iterations).

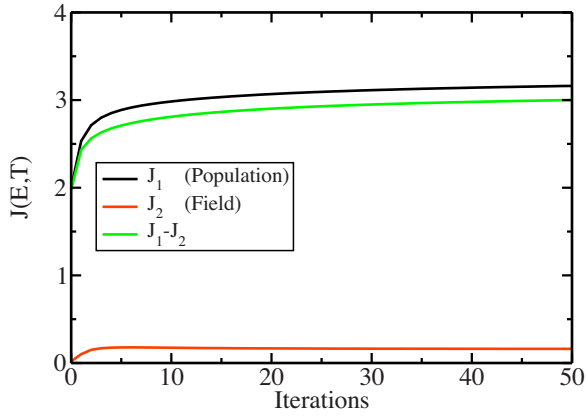

FIG. 8. Control functional as a function of iterations for the 6D model of ammonia ($J_1=4 \equiv 100\%$ population transfer for each target).

Unlike in the previous example only a single frequency component of optimal field centered around 960 cm^{-1} is visible. This frequency corresponds to the transition frequency between the $|10\rangle$ and $|11\rangle$ states at 962.77 cm^{-1}. As is the 3D case, a direct transition between these states is possible through the interaction with the electric field. Interestingly, the field envelope is (except during the first 350 fs) quite similar to the one for the filtered field obtained using the 3D model while the average field strength is slightly larger ($J_2=0.161$).

In Fig. 9, the population of those states with a population larger then 1% upon interaction with the optimal field is depicted as a function of time. In general, the population dynamics resemble those obtained with the 3D model and the filtered field. The critical difference is that the target population at the final time is much lower than in the previous case for the 3D model.

In Figs. 9(a) and 9(b), with $|10\rangle$ and $|11\rangle$ being the initial states, respectively, the target population at the final time is in both cases about 79%. Unlike in the previous example, also a larger amount of population is transferred outside the qubit system to the asymmetric ground state of the inversion mode $|0,0^-,0^0,0^0\rangle$. This contribution however almost vanishes at the final time.

As in the 3D case, a large amount of population transfer between $|00\rangle$ and $|01\rangle$ is observed. This results from a relatively strong transition dipole between those two states at 949 cm^{-1}, which is very close to the transition frequency between $|10\rangle$ and $|11\rangle$ at 962 cm^{-1}.

In Figs. 9(c) and 9(d) the population dynamics are shown for the initial states $|10\rangle$ and $|11\rangle$, respectively. As in the previous case approximately 80% population has been transferred to the target states. A small amount of population has also been transferred to the asymmetric ground state of the inversion mode $|0,0^-,0^0,1^1\rangle$ during the pulse, however, this time with one quanta of excitation in the asymmetric bending mode.

Compared to the 3D model much less population of the target states can be achieved within the 6D model. One reason for this is probably the small difference in the transition frequencies between the states $|00\rangle$, $|01\rangle$ and $|10\rangle$, $|11\rangle$, as well as a small difference in the respective transition dipoles. Also the transfer to the asymmetric ground state of the inversion mode may influence the optimization process.

It is interesting to note that within the 6D model no spurious frequencies appeared within the optimal field. Since the number of relevant transitions from the qubit states within the 6D model is the same as in the 3D model due to selection rules, the spurious contributions are likely to be suppressed due to smaller transition frequencies. For longer pulses with less spectral broadening (not shown here) additional frequencies also appear within the 6D model.

V. SUMMARY AND CONCLUSIONS

A combined approach of OCT and MCTDH has been used to calculate the optimal field for performing a CNOT quantum gate in ammonia. Results from a 3D model of am-

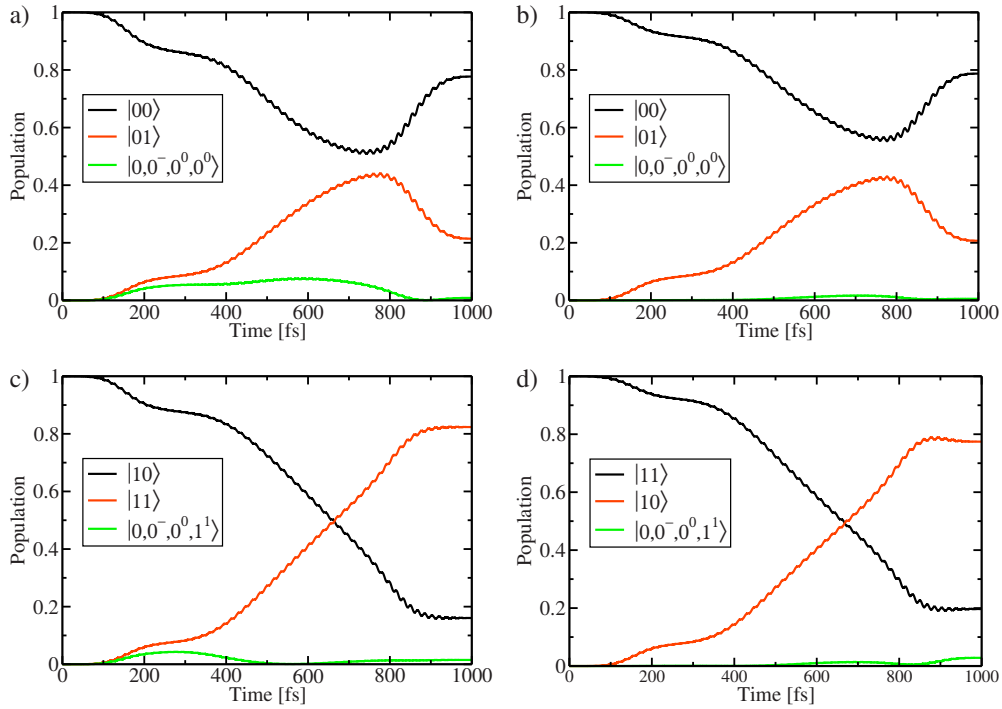

FIG. 9. Same as Fig. 4 but for the 6D model of ammonia.

monia and those from a full-dimensional model including all six internal vibrational DOF have been compared.

In the case of the 3D model, an average target population of 99.2% could be achieved with a 1 ps pulse. This is quite similar to the results obtained in Ref. 17 where a two-dimensional model of ammonia is utilized, however, with different definitions of qubit states. The obtained pulse contained substantial contributions at frequencies not needed within the optimal field. These contributions could be identified as artifacts of the control algorithm, which lead to a much more complicated form of the pulse. Filtering out the spurious frequencies leads to a simpler pulse, which only slightly reduced the final target populations. Using a different control algorithm with spectral restrictions of the field as proposed earlier[26] could be one possibility to suppress spurious frequencies.

In the case of the 6D model, an average target population of about 79% could be reached for a similar setup, i.e., the controllability of the 6D model is lower than for the reduced dimensionality model. One reason for this can be seen in the relatively low difference of the transition frequencies between the states $|00\rangle$, $|01\rangle$ and $|10\rangle$, $|11\rangle$ and the respective transition dipoles within the 6D model. That is, steering the two competing transitions by varying the field intensity is not as effective as in the 3D case. These circumstances therefore would require a different choice of the qubit system and/or a longer pulse. The pulse obtained using the 6D model has a similar shape as the filtered pulse obtained from the 3D calculation, exhibiting similar and, due to the direct transitions to the target states, relatively simple mechanisms for population transfer.

For universal quantum computing, Tesch and de Vivie-Riedle suggested[41] that a transition for the superposition state must be optimized in addition to the transitions given in Eq. (8), i.e.,

$$|00\rangle + |01\rangle + |10\rangle + |11\rangle \quad \rightarrow (|00\rangle + |01\rangle + |11\rangle + |10\rangle)e^{i\phi}, \tag{11}$$

in order to ensure a phase-correct quantum gate. A phase-correct quantum CNOT gate has not been determined in the present work as an accurate and reliable prediction of any quantum gate would also require the inclusion of rotational DOF. The primary results of this paper are the comparison between the reduced- and full-dimensionality vibrational models and the discussion of the origin of spurious frequencies in the OCT algorithm rather than a prediction of the field required for a CNOT gate for quantum computing.

In summary we note that we obtained relatively similar results for the optimal pulses within the 3D and the 6D models of ammonia, which lead to relatively similar mechanisms of population transfer. However, the final target population has been somewhat different in both cases and using the reduced model failed to predict the controllability of the full-dimensional model such that a precise description of the systems under consideration seems to be essential.

ACKNOWLEDGMENTS

We thank Hans-Dieter Meyer (University of Heidelberg) for providing us the source code of the MCTDH package and the Thiel-Group for providing us their potential energy- and dipole-surfaces of ammonia. The authors thank the Alberta Ingenuity Fund (New Faculty Award) and NSERC for financial support as well as the Canadian Foundation for Innovation (New Opportunities Fund) for support for computational infrastructure.

[1] A. P. Peirce, M. A. Dahleh, and H. Rabitz, Phys. Rev. A **37**, 4950 (1988).
[2] R. Kosloff, S. A. Rice, P. Gaspard, S. Tersigni, and D. J. Tannor, Chem. Phys. **139**, 201 (1989).
[3] W. Zhu, J. Botina, and H. Rabitz, J. Chem. Phys. **108**, 1953 (1998).

[4] W. Zhu and H. Rabitz, J. Chem. Phys. **109**, 385 (1998).
[5] T. Mančal, U. Kleinekathöfer, and V. May, J. Chem. Phys. **117**, 636 (2002).
[6] H. Rabitz, R. de Vivie-Riedle, M. Motzkus, and K. Kompa, Science **288**, 824 (2000).
[7] H. Rabitz, Theor. Chem. Acc. **109**, 64 (2003).
[8] G. Balint-Kurti, S. Zou, and A. Brown, Adv. Chem. Phys. **138**, 43 (2008).
[9] J. Konradi, A. K. Singh, and A. Materny, Phys. Chem. Chem. Phys. **7**, 3574 (2005).
[10] C. M. Tesch and R. de Vivie-Riedle, Phys. Rev. Lett. **89**, 157901 (2002).
[11] D. Babikov, Chem. Phys. **121**, 7577 (2004).
[12] Y. Ohtsuki, Chem. Phys. Lett. **404**, 126 (2005).
[13] T. Cheng and A. Brown, J. Chem. Phys. **124**, 144109 (2006).
[14] K. Shioya, K. Mishima, and K. Yamashita, Mol. Phys. **105**, 1283 (2007).
[15] U. Troppmann, C. M. Tesch, and R. de Vivie-Riedle, Chem. Phys. Lett. **378**, 273 (2003).
[16] M. Schröder, J.-L. Carréon-Macedo, and A. Brown, Phys. Chem. Chem. Phys. **10**, 850 (2008).
[17] S. Suzuki, K. Mishima, and K. Yamashita, Chem. Phys. Lett. **410**, 358 (2005).
[18] D. E. Goldberg, *Genetic Algorithms in Search, Optimization, and Machine Learning* (Addison-Wesley, Reading, 1989).
[19] R. Judson and H. Rabitz, Phys. Rev. Lett. **68**, 1500 (1992).
[20] J. Geremia, W. Zhu, and H. Rabitz, J. Chem. Phys. **113**, 10841 (2000).
[21] H.-D. Meyer, U. Manthe, and L. Cederbaum, Chem. Phys. Lett. **165**, 73 (1990).
[22] U. Manthe, H.-D. Meyer, and L. Cederbaum, J. Chem. Phys. **97**, 3199 (1992).
[23] M. H. Beck, A. Jäckle, G. A. Worth, and H.-D. Meyer, Phys. Rep. **324**, 1 (2000).
[24] H.-D. Meyer and G. A. Worth, Theor. Chim. Acta **109**, 251 (2003).
[25] L. Wang, H.-D. Meyer, and V. May, J. Chem. Phys. **125**, 014102 (2006).
[26] C. Gollub, M. Kowalewski, and R. de Vivie-Riedle, Phys. Rev. Lett. **101**, 073002 (2008).
[27] Y. Ohtsuki, G. Turinici, and H. Rabitz, J. Chem. Phys. **120**, 5509 (2004).
[28] Y. Ohtsuki, Y. Teranishi, P. Saalfrank, G. Turinici, and H. Rabitz, Phys. Rev. A **75**, 033407 (2007).
[29] W. Zhu and H. Rabitz, J. Chem. Phys. **118**, 6751 (2003).
[30] C. Iung and F. Gatti, Int. J. Quantum Chem. **106**, 130 (2006).
[31] F. Gatti, C. Muñoz, and C. Iung, J. Chem. Phys. **114**, 8275 (2001).
[32] H.-D. Meyer, F. L. Quéré, C. Léonard, and F. Gatti, Chem. Phys. **329**, 179 (2006).
[33] S. N. Yurchenko, J. Zheng, H. Lin, P. Jensen, and W. Thiel, J. Chem. Phys. **123**, 134308 (2005).
[34] S. N. Yurchenko, M. Carvajal, H. Lin, J. Zheng, W. Thiel, and P. Jensen, J. Chem. Phys. **122**, 104317 (2005).
[35] F. Gatti and C. Iung, J. Theor. Comput. Chem. **2**, 507 (2003).
[36] Š. Urban, V. Špirko, D. Papoušek, J. Kauppinen, S. P. Belov, L. I. Gershtein, and A. F. Krupnov, J. Mol. Spectrosc. **88**, 274 (1981).
[37] C. Cottaz, I. Kleiner, G. Tarrago, L. R. Brown, J. S. Margolis, R. L. Poynter, H. M. Pickett, T. Fouchet, P. Drossart, and E. Lellouch, J. Mol. Spectrosc. **203**, 285 (2000).
[38] I. Kleiner, G. Tarrago, and L. R. Brown, J. Mol. Spectrosc. **173**, 120 (1995).
[39] J. M. Hollas, *Modern Spectroscopy* (Wiley, West Sussex, 2004).
[40] S. Linden, H. Giessen, and J. Kuhl, Phys. Status Solidi B **206**, 119 (1998).
[41] C. M. Tesch and R. de Vivie-Riedle, J. Chem. Phys. **121**, 12158 (2004).